Nanoscale

Accepted Manuscript

Nanoscale

rsc.li/nanoscale

Volume 10
Number 4
28 January 2018
Pages 1549-2172

ISSN 2040-3372

ROYAL SOCIETY
OF CHEMISTRY

NCNST

PAPER
Shuping Xu, Chongyang Liang et al.
Organelle-targeting surface-enhanced Raman scattering
(SERS) nanosensors for subcellular pH sensing

ROYAL SOCIETY
OF CHEMISTRY

rsc.li/nanoscale

Binding of Polar and Hydrophobic Molecules at the LiCoO$_2$ (001)-water Interface: Force Field Development and Molecular Dynamics Simulations

Dongyue Liang,[†] Juan Liu,[‡,¶] Hendrik Heinz,[‡] Sara E. Mason,[§] Robert J. Hamers,[∥] and Qiang Cui*[,⊥]

[†]*Department of Chemistry and Theoretical Chemistry Institute, University of Wisconsin-Madison, 1101 University Avenue, Madison, WI 53706*

[‡]*Department of Chemical and Biological Engineering, University of Colorado-Boulder, Boulder, CO 80303-0596*

[¶]*Department of Materials Science and Engineering, Dalian Maritime University, Dalian, Liaoning 116026, China*

[§]*Department of Chemistry, University of Iowa, E331 Chemistry Building, Iowa City, Iowa 52242*

[∥]*Department of Chemistry, University of Wisconsin-Madison, 1101 University Avenue, Madison, WI 53706*

[⊥]*Departments of Chemistry, Physics and Biomedical Engineering, Boston University, 590 Commonwealth Avenue Boston, MA 02215*

E-mail: qiangcui@bu.edu, Tel:(+1)-617-353-6189

1

Abstract

A classical model in the framework of the INTERFACE force field has been developed for treating the LiCoO$_2$ (LCO) (001)/water interface. In comparison to *ab initio* molecular dynamics (MD) simulations based on density functional theory, MD simulations using the classical model lead to generally reliable descriptions of interfacial properties, such as the density distribution of water molecules. Water molecules in close contact with the LCO surface form a strongly adsorbed layer, which leads to a free energy barrier for the adsorption of polar or charged molecules to the LCO surface. Moreover, due to the strong hydrogen bonding interactions with the LCO surface, the first water layer forms an interface that exhibits hydrophobic characters, leading to favorable adsorption of non-polar molecules to the interface. Therefore, despite its highly polar nature, the LCO (001) surface binds not only polar/charged but also non-polar solutes. As an application, the model is used to analyze the adsorption of reduced nicotinamide adenine dinucleotide (NADH) and its molecular components to the LCO (001) surface in water. The results suggests that recently observed redox activity of NADH at the LCO/water interface was due to the co-operativity between the ribose component, which drives binding to the LCO surface, and the nicotinamide moiety, which undergoes oxidation.

1   Introduction

Transition metal oxides hold great promise as novel electrode materials.[1–3] As the scale of their production further expands, questions regarding their long-term environmental impacts have started to attract an increasing level of concern.[4] As an example, $LiCoO_2$ (LCO) and its broader family of "NMC" ($LiNi_xMn_yCo_{1-x-y}O_2$) oxides[5] have been observed to undergo dissolution in water solution, and the released transition metal ions and resulting reactive oxygen species (e.g., OH radical) led to toxicity to biological systems.[6,7] To alleviate the negative environmental impacts, it is important to understand the interaction between these metal oxides with various molecules frequently encountered in the environment or biological milieu, as well as the impact of the interaction on the dissolution process. Increasing amount of efforts have been spent along this line,[6–10] although much remains to be learned regarding the microscopic mechanisms, including the binding selectivity towards polar, charged and hydrophobic molecules at the metal oxide/water interface.

To understand the physical principles that govern binding selectivity at the metal oxide/water interface, computational studies[11–13] are promising yet not technically straightforward. Since the binding of charged and hydrophobic molecules is expected to perturb the local hydration environment,[14,15] explicit solvent simulations are preferable to implicit solvent models,[16,17] especially for binding kinetics. Explicit solvent simulations with quantum mechanical potential functions are computationally demanding, and state-of-the-art simulations typically reach 10-100 picoseconds of sampling,[18,19] which is usually not sufficient for converging binding free energies.[14] Molecular dynamics simulations using empirical force fields are much more affordable, but parameterization of reliable force fields for metal oxide/water interface requires considerable amount of efforts, although largely automated machine learning techniques have been shown to be promising in recent studies.[20,21]

In this work, building on a recently parametrized LCO force field that is compatible with popular biological force fields like CHARMM[22,23] and Amber,[24] we develop an updated model suitable for simulating LCO/water interface (001 surface) under the neutral pH condi-

tion. We calibrate the model by comparing computed surface features to *ab initio* molecular dynamics simulations, and then apply it to study the binding affinities of a set of small molecules of different physicochemical properties. Finally, we use the model to better understand recent experimental studies[10] of reduced nicotinamide adenine dinucleotide (NADH) binding and reactivity at the LCO surface in water.

2   Computational Methods

The starting force field model for our treatment of the LCO/water interface is the bulk metal oxide force field of Heinz, Jain and co-workers.[25] We made revision of that model to consider the termination pattern of the LCO (001) surface at neutral pH, and developed parameters for the new atom types by DFT calculations and following the standard protocol for CHARMM force field parameterization.[22] Description of the LCO/water interface is then compared to DFT molecular dynamics simulations. Finally, we apply the force field model to study the binding of small molecules and NADH to LCO in water.

2.1   Force field parametrization

To obtain benchmark data for the parametrization of surface termination atoms, plane wave DFT calculations are carried out with Quantum Espresso 6.3.[26,27] Two 50% hydrogen-terminated LCO systems (see below) are optimized for the DFT calculations, where the smaller system (24 atoms) is used for the initial Bader charge analysis,[28–30] and the larger system (192 atoms) for the energy scan calculations. Both set-ups contain only one orthogonal cell along the z dimension (~ 14 Å), and the z dimension of simulation box is set to be 35 Å to leave gaps between the oxide surfaces through their periodic images; the $x - y$ dimensions are approximately 9.85 Å$\times$11.37 Å for the larger system. The PBE functional[31] is applied with the Hubbard U correction[32] on Cobalt atoms, for which a Hubbard U value of 5.0 eV is used.[33] A kinetic energy cutoff of 40 Ry is applied, and 320 Ry is applied for

charge density and potential; k points are sampled with a 4×4×1 scheme. Ultrasoft pseudopotentials[34,35] are applied to account for the effects of core electrons. Gaussian smearing is enabled with a degauss parameter of 0.01 Ry. Overall, the set-up of plane wave DFT calculations is consistent with previous simulations reported by Mason and coworkers.[36,37]

To obtain the force field parameters for the new atom types (see Set.3.1), we minimize the mean square deviation between the force field and DFT results for the interaction between LCO and a water molecule in potential energy scans. For the optimization of force field parameters, we utilize a simplex algorithm with the Nelder-Mead method,[38] which is part of the SciPy distribution.[39] The classical force field calculations required for the potential energy scans are performed with the CHARMM package.[40] Particle mesh Ewald[41] is applied for electrostatics with a non-bonded cutoff distance of 12 Å. Force switch functions are applied with a switching distance of 10 Å.

2.2 Ab initio molecular dynamics

To benchmark the performance of the force field, *ab initio* MD (AIMD) simulations are carried out with the hybrid Gaussian/Plane wave (GPW) DFT.[42] The simulation system contains 192 atoms for the 50% hydrogen-terminated LCO (001) surface and water (see below), summing up to 531 atoms in total. The Born-Oppenheimer MD simulations are performed with the CP2K package.[43] The PBE functional[31] is applied with the Grimmes D3 empirical correction.[44] The GTH (Goedecker-Tetter-Hutter) pseudopotentials and DZVP-MOLOPT-SR basis sets are applied to all atoms. A multigrid cutoff of 500 Ry and a relative cutoff of 40 Ry are applied. The simulation is carried out at the temperature of 300 K with the Nose-Hoover thermostat. All hydrogen atoms in the simulation are substituted by deuterium to allow the use of a larger time step of 0.5 fs.

2.3   Classical molecular dynamics

All classical MD simulations are performed using the NAMD package[45] with GPU acceleration, unless specified otherwise. For unbiased MD simulations, the system size is approximately $80\times92\times106$ Å^3 (orthorhombic cell) for all small molecule adsorption systems. The size of the system with only LCO and water is approximately $30\times35\times43$ Å^3. All classical MD systems except the water-only system are solvated with 0.15M NaCl. Water and salt ions in the classical MD simulations are treated using the modified TIP3P model[46,47] and CHARMM models,[48] respectively; we note that specific Na$^+$-Cl$^-$ non-bonded parameters (NBFIX) developed based on osmotic pressure calculations[49] are used. Langevin dynamics with a damping coefficient of 1 ps^{-1} is applied for constant temperature control at 300 K. Particle mesh Ewald[41] is applied to electrostatics. The non-bonded cutoff is set to be 12 Å, together with a switching distance of 10 Å. Langevin piston[50] is used for pressure coupling for all three dimensions with a targeting pressure of 1 atm. The box sizes in x and y dimensions, along which the oxide material is periodic, change little throughout the simulations. Along the z direction, the water distribution from the classical MD simulations exhibits bulk regions with the expected density. For LCO-water only system, for example, the bulk density of water is 1.002 g/cm^3, which validates the barostat used in this work.

In addition to long, unbiased MD simulations that involve multiple copies of small molecules near the LCO surface in water, metadynamics[51] is used to explicitly characterize the free energy surface of small molecule adsorption onto the LCO surface. Two collective variables, the vertical distance between the centers of mass from LCO to the small molecule and the water coordination number of 4 selected surface oxygen atoms (see Fig. S2), are used in the metadynamics. The coordination number between two groups, G_1 and G_2, is described with the following function:

$$\#Coord(G_1, G_2) = \sum_{i\in G_1}\sum_{j\in G_2}\frac{1-(|\mathbf{x_i}-\mathbf{x_j}|/d_0)^n}{1-(|\mathbf{x_i}-\mathbf{x_j}|/d_0)^m} \tag{1}$$

where d_0 is 3.0 Å, n and m are set to 6 and 12, respectively (see Fig. S3 for additional discussion on the coordination number collective variable). The grid widths of collective variables are set to be 0.2 Å and 0.1, respectively. The height of each hill used for metadynamics is set to be 0.1 kcal/mol, with a depositing frequency of 1 ps. The hill width is set to be 1 grid size. Well-tempered metadynamics[52] is enabled with a bias temperature of 15,000 K. Harmonic wall potentials are applied to limit the sampling to a cylindrical region around the surface binding site, with a radius of 4 Å and a radial force constant of 200 $kcal \cdot mol^{-1} Å^{-2}$; an upper wall is placed at the vertical center of mass distance of 15 Å with a force constant of 8 $kcal \cdot mol^{-1} Å^{-2}$.

3　Results and Discussions

3.1　Force field parametrization

The LCO force field reported in this work is a modified version by Heinz, Jain and coworkers[25] in the INTERFACE force field framework, which is designed to be compatible with commonly used non-polarizable force fields, e.g., CHARMM[22,23] and Amber,[24] and common water models, e.g., TIP3P[46,53] and SPC/E.[54,55] Bonded interactions are defined between Co and O atoms, while the Li atoms only interact through non-bonded interactions. The oxygen atoms in LCO are classified into two types by layer, denoted as O1 and O2 in this work (see Fig. 1a). While the O1 and O2 atom types are identical in non-bonded parameters and bonded parameters with Co, this classification allows different angle parameters; i.e., the angle parameters for O1-Co-O1/O2-Co-O2 are different from that for O1-Co-O2. No dihedral or other type of bonded interactions are defined. In the original work reported by Heinz, Jain and coworkers,[25] the obtained parameters were benchmarked against a series of bulk properties, e.g., lattice parameters and mechanical moduli, and excellent agreement with experimental measurements was observed. To validate the use of the force field for interfaces, the authors further benchmarked the model for cleavage energy, which showed

good agreement with DFT calculation.

However, when LCO is in water solution, the surface termination of the exposed oxygen layer is expected to be different from a cleanly cleaved surface. With plane wave DFT plus implicit solvation calculations, Mason and coworkers compared different surface termination patterns and predicted that 50% hydrogen termination (evenly distributed) for the exposed oxygen layer as the most stable configuration under neutral pH.[36] Therefore, to parametrize for LCO/water interfaces, we performed plane wave DFT calculation on the 50% hydrogen terminated surface. With the Bader charge analysis, it is observed that the charges on the terminating layer oxygen atoms are significantly different from those in the bulk, while the charges on cobalt are rather uniform. Therefore, we propose three additional atom types for non-bonded interactions, which are terminating oxygen (OT), terminating hydrogen (HT), and the oxygen atom bonded to terminating hydrogen (OH); see Fig. 1a. Since the oxygens in different layers are labeled as different names to define the angle parameters in the original bulk force field, the three new non-bonded atom types bring in five new atom names (OH1, OH2, OT1, OT2, HT) in total. It is also found that, although the charges obtained from Bader analysis are substantially different from the charge parameters developed by Heinz et al., the ratios between the two sets of charges are consistent among different atom types. Thus, the Bader charges scaled by the weighted-average ratio are proposed as the initial set of charge parameters for the new atom types (see Table S1 in **Supporting Information** for charges and additional discussions).

To fine tune the force field parameters for the new atom types, we first optimize two representative hydrogen bonding structures between a water molecule and the terminated LCO surface using DFT. Starting from the optimized structure, a potential energy scan for the interaction between the water molecule and the surface is performed by varying the position of the water molecule along the vertical direction away from the surface at the DFT level. In the energy scan, both the surface and and the water molecule retain their optimized structures, and only the vertical separation between the two is varied. Using a

8

simplex algorithm, the mean square deviation between force field calculated and reference interaction energies is minimized to obtain the optimized force field parameters for the new atom types (See Fig. 1). During such optimization, only the non-bonded parameters (charge, Lennard-Jones parameters) of the newly added atom types (non-bonded parameters for OT1 and OT2, OH1 and OH2 are the same, only 3 new atom types are required for the parametrization here) are set to vary. In the force field calculations, the TIP3P model is used for water to ensure the compatibility of the resulting LCO force field with CHARMM. The optimized non-bonded parameters are listed in Table 1. Note that the charge parameters are not significantly different from the proposed parameters based on scaled Bader charges. For the bonded terms, only a few parameters of the termination-related atom types are added (See Table 2).

Table 1: Optimized non-bonded parameters (ϵ in kcal/mol, $R_m/2$ in Å and and q in e) for the new atom types in the LCO force field for interfacial systems.

Type	ϵ	$R_m/2$	q
Li	-0.04	0.97	0.641
Co	-0.04	2.52	0.962
O1	-0.15	1.94	-0.798
O2	-0.15	1.94	-0.798
OH1	-0.189	1.43	-0.848
OH2	-0.189	1.43	-0.848
OT1	-0.167	1.58	-0.624
OT2	-0.167	1.58	-0.624
HT	-0.036	0.24	0.492

3.2 Interfacial water structure

To benchmark the force field model for predicting interfacial interactions, we perform AIMD at the RPBE-D3 level for 50 ps in total, where the first 10 ps is not used for analysis, and compare the results to classical MD simulations of 10 ns. As shown in Fig. 2, the peak positions of the oxygen atoms in the oxide is not perfectly reproduced by the force field simulation, with a deviation of ~ 1 Å in z dimension. This is presumably due to the
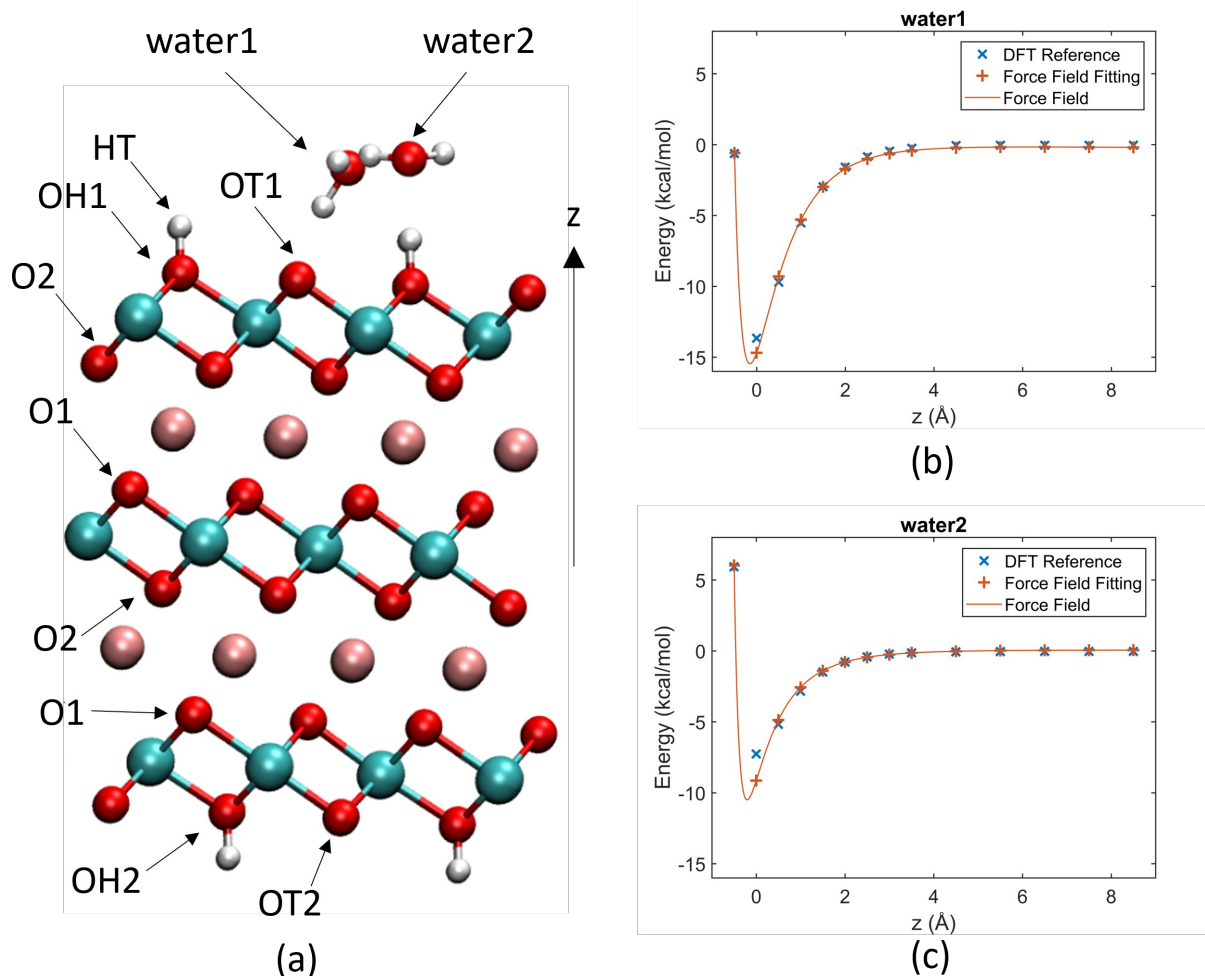
Figure 1: Parameterization of new atom types in the LCO force field for interfacial systems. The snapshot illustrates the key atom types in the revised LCO force field (OT1=OT2, OH1=OH2, HT; bulk oxygens such as O1 and O2 are treated using the original model of Heinz et al.[25]). To optimize the partial charges and LJ parameters for these atom types, the interaction energy between a water probe and LCO is compared between force field calculations and DFT results; two different types of LCO-water coordination are studied, as illustrated in the snapshot. Starting from the DFT optimized structure, the water probe is moved away from the surface in the z direction, leading to the energy curves shown on the right. The optimized force field parameters lead to almost identical energy curves as the DFT calculations in both attractive and repulsive regions of the potential energy curves.

Table 2: Additional bonded parameters of the LCO force field. Units of k_b, b_0, k_θ and θ_0 are $kcal \cdot mol^{-1} \mathring{A}^{-2}$, $\mathring{A}$, $kcal \cdot mol^{-1} \cdot rad^{-2}$ and degrees, respectively. No Urey-Bradly terms or additional dihedrals are defined.

Bond type	k_b	b_0
OH1-HT	545.0^a	0.97^b
OH2-HT	545.0^a	0.97^b
Angle type	k_θ	θ_0
Co-OH1-HT	30.0	122.27^b
Co-OH2-HT	30.0	122.27^b

a. Taken from the OG311-HGP1 type in the CHARMM CGENFF force field.[56] b. From plane wave DFT optimized structure. See Fig. S1 for comparison between plane wave DFT and force field for the relevant angle bending potential energy profile.

difference between parametrization conditions, since the bulk properties were parametrized with 3-dimensional periodicity.[25] However, the interfacial water distributions between *ab initio* and classical MD simulations generally agree well in terms of density peak values and positions, although the *ab initio* results exhibit larger fluctuations due to the short trajectory.
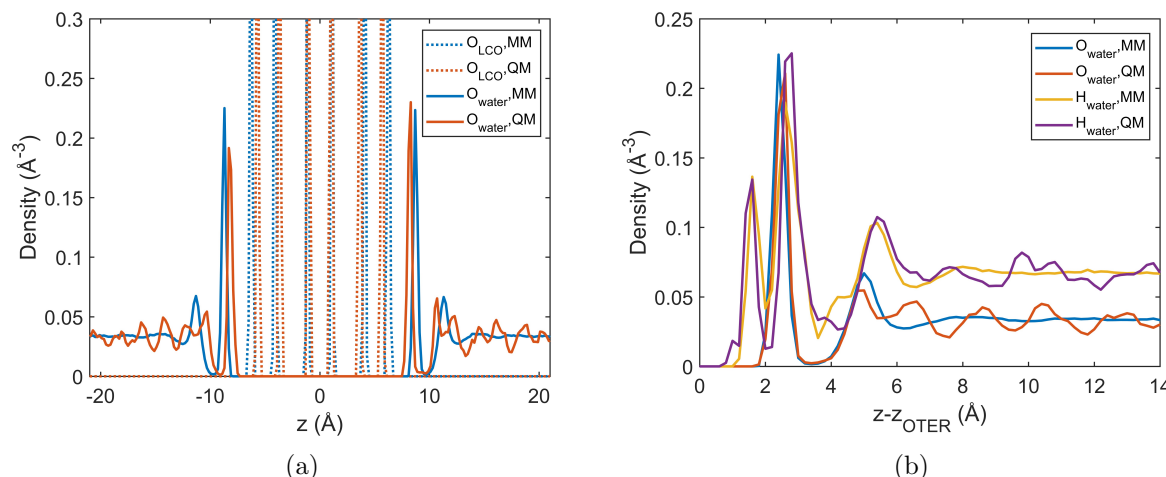

Figure 2: Comparison of interfacial structure for the LCO(001)-water interface from *ab initio* and classical MD simulations. (a) Number densities profiles for selected atoms from 50 ps *ab initio* and 10 ns classical MD simulations, where z is defined as the vertical distance between centers of mass of LCO and the atom type of interest. (b) shows the water distribution with respect to $z - z_{OTER}$, and z_{OTER} is the average position of the terminating oxygen atoms. The profiles are averaged over both surfaces of LCO.

As shown in the interfacial water density profile (Fig. 2), the first layer of water is $\sim$

2.5 Å away from the terminating layer of oxide oxygen atoms, and the peak height is $\sim$ 6 times of the bulk water density; the latter trend is consistent with previous AIMD study of metal oxide surfaces, such as TiO_2, which also exhibited a first layer water density that is 5-6 times of the bulk value.[57] The interfacial distribution of water hydrogens shows two peaks, indicating that the first layer waters do not form a 2-dimensional structure like those in contact with hydrophobic surfaces.[15] This is expected as the first layer of water can form directed hydrogen bonds with the LCO surface, as shown in the snapshot in Fig. 3a. The water density profile also shows a second peak of oxygens at $\sim$ 5 Å, which is significantly wider and lower than the first peak. The snapshot also supports that the second layer is less structured than the first layer of water.


(a)   (b)
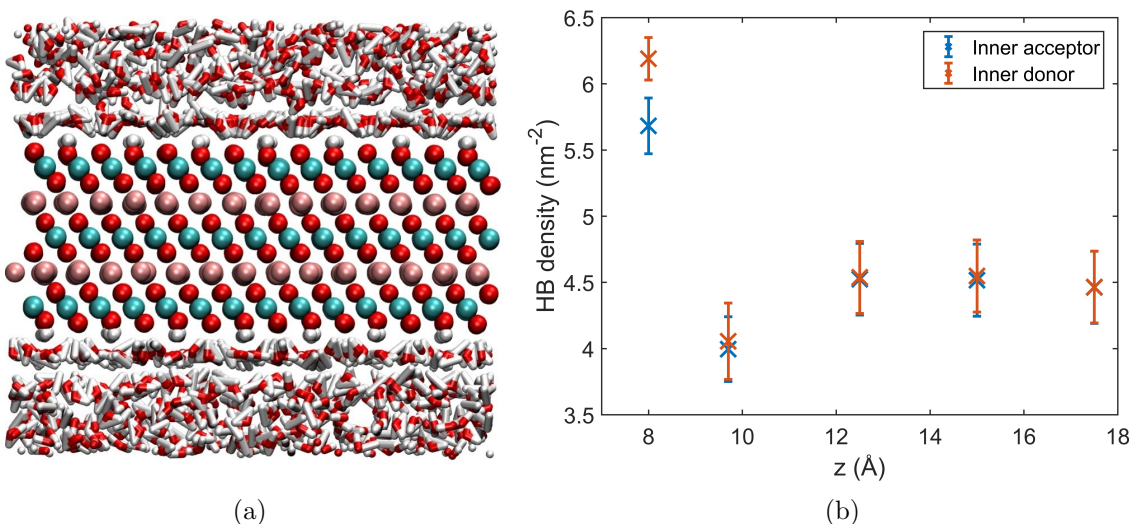
Figure 3: Water structure at the LCO (001)-water interface. (a) A snapshot from classical MD simulation and (b) cross-plane hydrogen bonding density at selected planes. The first few locations in (b) on the z axis are selected to be (from left to right) between the terminating atoms of LCO and the first-layer waters (z = 8.0 Å), between the first-layer and second-layer waters (z = 9.7 Å), between the second-layer water and beyond (z = 12.5 Å). The later positions are selected to be z = 15.0 and 17.5 Å for comparison. The distance (O $\cdots$ O) and angular (O $\cdots$ H $\cdots$ O) criteria for identifying hydrogen bonds are set to be 3.2 Å and 140°, consistent with Ref. 15.

In numerous studies, water molecules at certain interfaces, such as metal surfaces and hydrophobic surfaces, were shown to exhibit hydrophobic characters due to the formation

of two-dimensional hydrogen-bonding networks.[58–60] Motivated by these discussions, we analyze the hydrogen bonding network of water molecules at the LCO/water interface. The numbers of cross-plane hydrogen bonds are shown in Fig. 3b (see the caption for detailed identifications of the planes). It is clearly observed that the LCO surface and the first-layer waters form significantly more hydrogen bonds than any other inspected water layers. This leads to a decrease of hydrogen bonding between the first and second layers to ~ 8 hydrogen bonds per nm^2, as compared to the bulk value of ~ 9. The hydrogen bonding between second-layer water and beyond is not significantly perturbed from the bulk. Moreover, we observe that there are 1.08 ± 0.02, 1.68 ± 0.06 and 0.74 ± 0.04 hydrogen bonds per molecule formed between LCO surface and the first-layer water, among the first-layer waters, and between the first- and second-layer waters. These values can be compared to those from the study of Pizzoti and coworkers, who reported similar analysis of water molecules near a gold surface,[15] and their values are 0, 2.9 and 0.4, respectively. While the total number of hydrogen bonds formed per water molecule is similar in the two systems, waters at gold surface do not form hydrogen bonds to gold and therefore form significantly more intra-layer hydrogen bonds in a two-dimentional network. As a result, the first-layer waters form fewer hydrogen bonds with the second-layer waters, leading to a more hydrophobic first water layer as compared to the case of LCO/water interface.

3.3 Interfacial adsorption of molecules

To understand factors driving interfacial adsorption at the LCO surface, we study acetic acid, acetate, benzene and methylammonium (Fig. 4a), denoted as ACEH, ACET, BENZ and MAMM in the CHARMM force field,[56] as representatives of polar, anionic, non-polar and cationic small adsorbates. We first study their binding to the LCO surface with unbiased classical MD simulations that contain 15 of each small molecules with randomized starting positions; the simulations are performed with 4 replicas with different starting positions of the small molecules, and each replica is run for 200 ns.
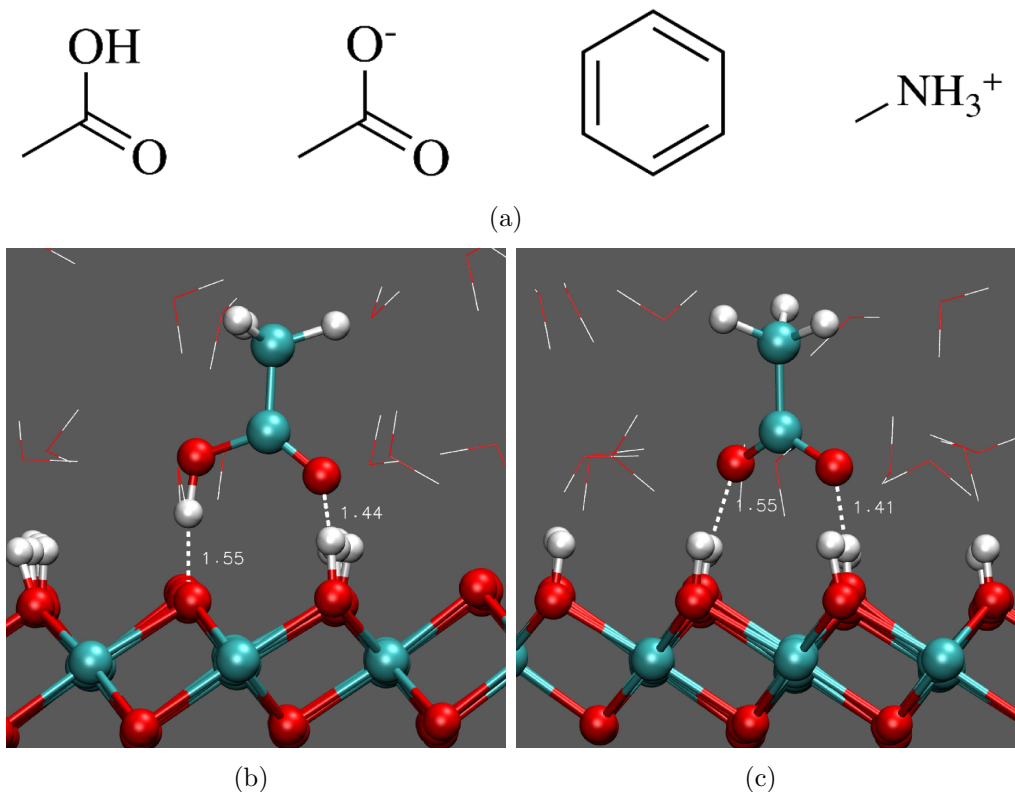
Figure 4: Adsorption of small molecules to the LCO(001)-water interface. (a) Structural formulas of small molecules studied in Sec. 3.3. From left to right: acetic acid (ACEH), acetate (ACET), benzene (BENZ), methylammonium (MAMM). (b,c) Snapshots of ACET (b) and ACEH (c) at free energy minimum positions at z ∼ 9-10 Å from well-tempered metadynamics (See Fig. 5 for PMFs). The hydrogen bonds between the small molecule and the surface are indicated with dashed lines.

Nanoscale Accepted Manuscript
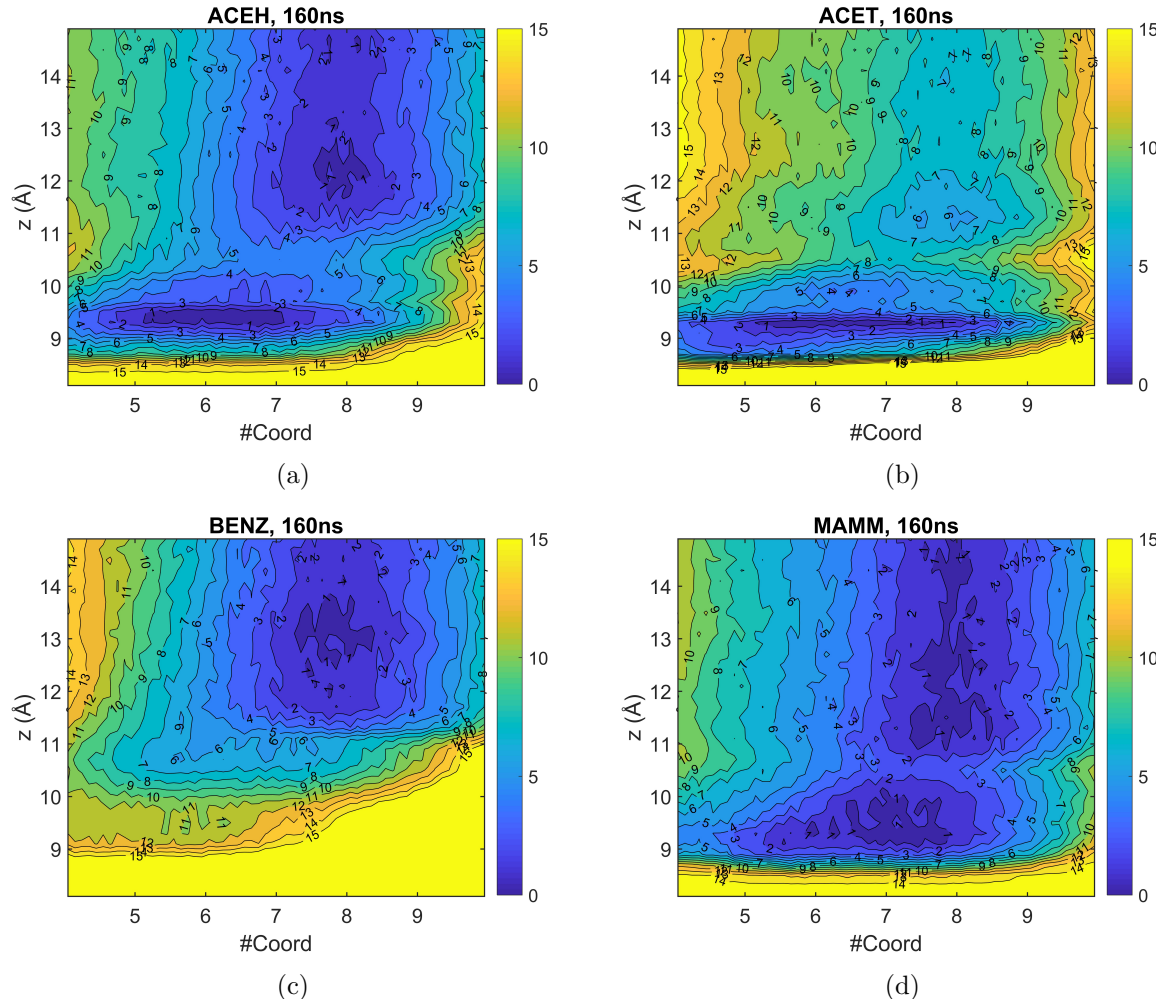
Figure 5: Two-dimensional PMFs (in the unit of kcal/mol) for the adsorption of small molecules to the LCO(001)-water interface from 160 ns well-tempered metadynamics. The two collective variables are z and #Coord, which are the vertical distance between centers of mass of the small molecule of interest and the LCO slab, and the water coordination number of a few selected surface oxygens of the LCO at the binding site (see Sec. 2.3 for details). Panels (a-d) represent results for acetic acid (ACEH), acetate (ACET), benzene (BENZ) and methylammonium (MAMM), respectively.

From the center of mass density distributions of the small molecules, a preferential adsorption order of ACET > ACEH > MAMM > BENZ is observed (Fig. S4a in **Supporting Information**). This trend is consistent with the 2-dimensional potential of mean force (PMF) maps from well-tempered metadynamics shown in Fig. 5, where the water coordination number to the surface binding sites is taken as the additional collective variable. One dimensional PMF where the vertical distance between centers of mass of the small molecule and LCO serves as the collective variable can be obtained straightforwardly from both types of simulations, as shown in Fig. S4b in **Supporting Information**. The binding affinities obtained from the two types of simulations are consistent in general, which are $\sim 3\ k_BT$, $2\ k_BT$ and less than $1\ k_BT$ for ACEH, MAMM and BENZ, respectively. The ACET binding affinities are significantly different, however, which are $\sim 5\ k_BT$ from unbiased MD and $\sim 13\ k_BT$ from metadynamics, respectively. The $\sim 5\ k_BT$ local minimum is observed at $z = 9.9$ Å in both PMFs, while the $\sim 13\ k_BT$ minimum is located at an inner location of $z = 9.3$ Å; the latter represents direct bi-dentate coordination between ACET and the surface, which apparently is accessible only in metadynamics simulations in which desorption of water from the binding site is explicitly sampled.

The PMF minima of ACET, ACEH and MAMM binding are all within the range of the first water layer, indicating that they are able to form direct contact with the surface terminating groups of LCO. The corresponding wells in 2-dimensional PMFs extend to regions with smaller water coordination numbers, which indicates that the small molecules take place of water molecules to form favorable contacts with the LCO surface. This is most obvious for the cases of ACET and ACEH, which are observed to form multiple stable hydrogen bonding interactions with the surface (see Fig. 4b for snapshots). The PMFs of these cases all show barriers outside the first water layer, which highlight the cost of local water rearrangement near the binding site. BENZ, however, is not able to form direct contact with the surface, and the PMF shows a small minimum at the location of the second water layer. This minimum is expected to reflect the hydrophobic nature of the first-layer water,

as discussed above.[58,60,61] The effects are expected to be even more significant with larger non-polar adsorbants, since their presence unavoidably breaks hydrogen bonds between water molecules, making the binding location of the second water layer the least disruptive in terms of hydrogen-bonding energetics. To explicitly illustrate this point, we set up a system where a single-layer graphene slab with the size of 10×10 $\mathring{A}^2$ is placed above the LCO/water interface. With MD simulations, it is observed that the graphene slab quickly settles to lie flat in the second water layer (See Fig. S6 in **Supporting Information**), indicating strong favorable interfacial binding despite the polar nature of the LCO surface.

3.4 Application to the adsorption of NADH and its molecular components at the LCO/water interface

The ion dissolution behavior of LCO in solution is expected to lead to redox reactions, since the released Co(III) is much less stable than Co(II) in water. Hamers and coworkers[10] studied the impact of nicotinamide adenine dinucleotide (NADH) and glutathione (GSH) on LCO and other Co battery materials, and found NADH and GSH to enhance ion dissolution. Further studies showed the binding of NADH to LCO, and the coupled transformation oxidized NADH to NAD$^+$. It was hypothesized that the nicotinamide moiety of NADH is responsible for the redox reaction and that the ribose phosphate is responsible for anchoring NADH to LCO. Accordingly, Hamers and coworkers designed experiments with 1-methyl-1,4-dihydronicotinamide ("NICO") and ribose 5-phosphate ("RIBO"), which were the key molecular fragments of NADH, and exposed them to LCO. Opposite to their expectation, RIBO was observed to reproduce the effects of NADH in enhancing ion dissolution, while NICO was not significantly oxidized upon exposure to LCO. These observations and the co-operativity between different parts of the NADH molecule in the redox process motivated the computational studies on the microscopic process of NADH/NICO/RIBO adsorption to LCO.

To compare the adsorption behaviors of NADH, NICO and RIBO to the LCO surface,
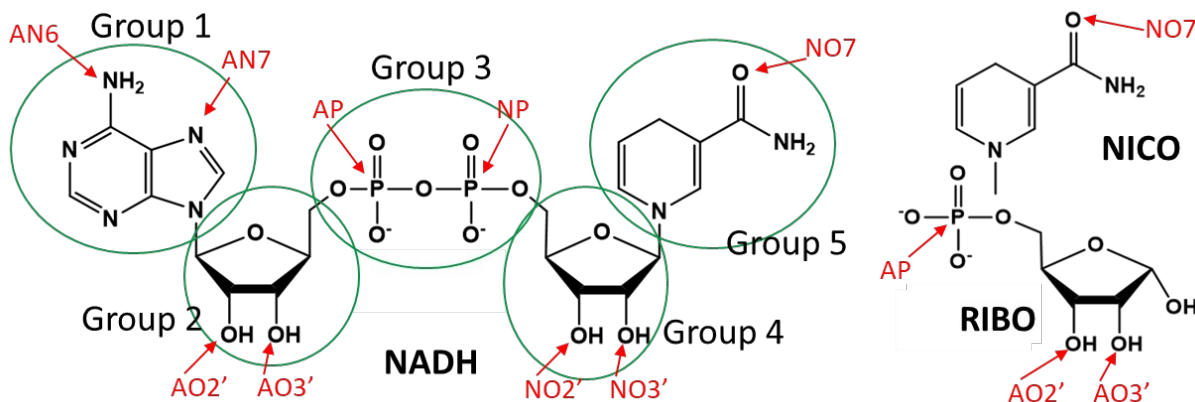
Figure 6: Structural formula of nicotinamide adenine dinucleotide (NADH), 1-methyl-1,4-dihydronicotinamide (NICO) and ribose 5-phosphate (RIBO). The NADH is divided into five groups in the binding analysis, and atoms used for defining the collective variables for PMFs (see Fig. 7) are labeled on the formula.

two types of systems, in which LCO is assembled with 15 NADH molecules or 15 NICO and RIBO each, are set up for MD simulations. Four replicas for each system are run for 500 ns each, summing up to 2 microseconds of trajectories for each set-up.

For the analysis, the NADH molecule is divided into 5 groups (see Fig. 6) to compare their binding behaviors. We monitor the minimum distance (see Table S2 in **Supporting Information** for detailed discussions) between any heavy atoms of each group in the NADH molecule and that of the LCO surface; a threshold of 2.7 Å is used for defining the binding interactions to the LCO surface. It is found that all 5 groups of NADH bind with the LCO surface. Group 3, which include the ribose, has the most binding counts among all groups.

We then convert the minimal distance distributions (Fig. S8) to binding PMFs, which are shown in Fig. 7. The collective variables are defined as the vertical distances between centers of mass of LCO and atoms identified based on the minimum distance analysis. Almost all PMFs have the first minima within 10 Å, indicating close contact with the surface. For the groups of NADH, the minima range from 2 k_BT to 4 k_BT; group 3 has the largest binding affinity of 4 k_BT among all groups. For RIBO, the ribose group shows much higher binding affinity of 8 k_BT compared to NADH groups. NICO, however, exhibits very little adsorption to the LCO surface. It has to be emphasized that the adsorption/desorption equilibrium is
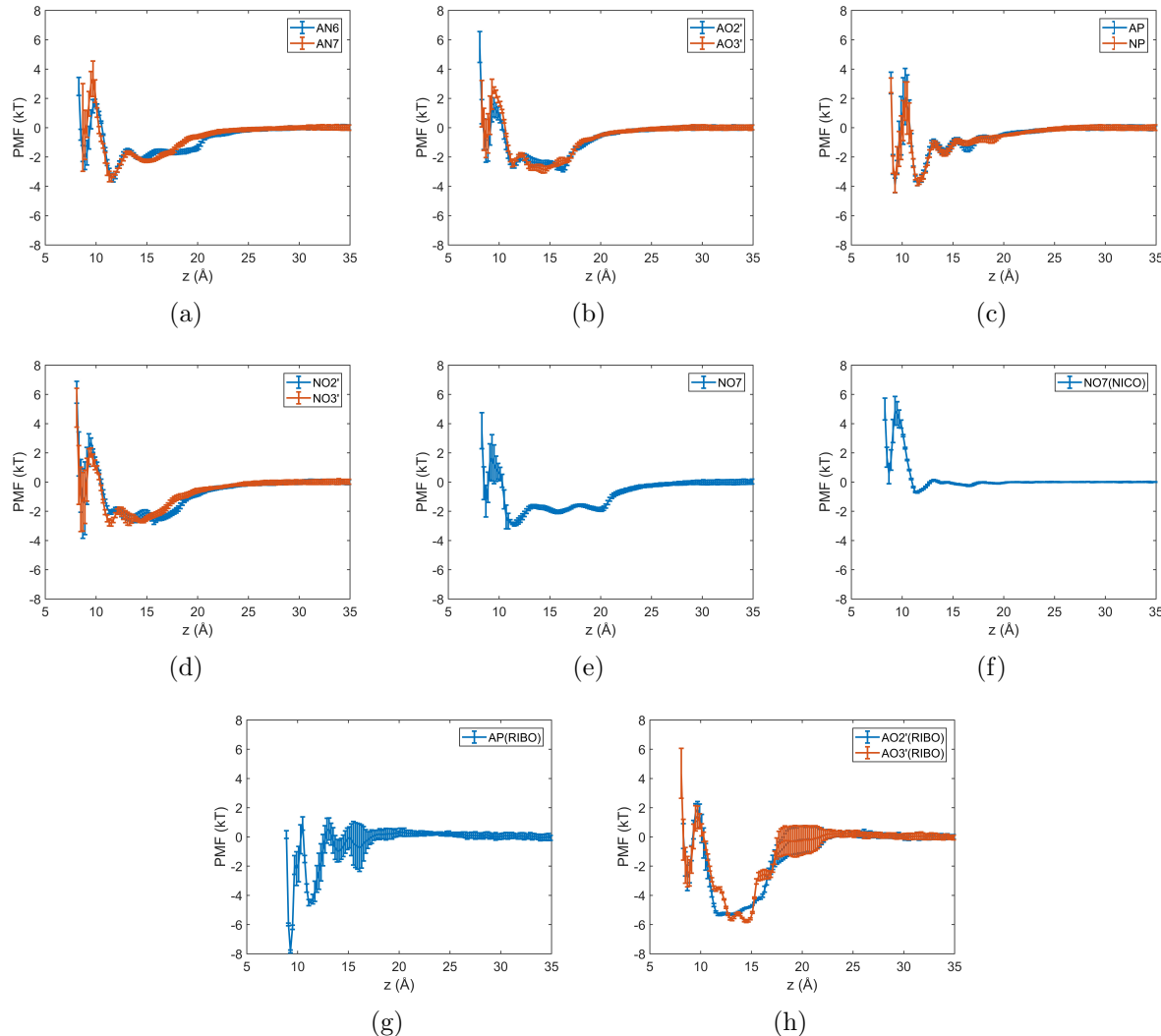
Figure 7: PMFs calculated from number density distributions (Fig. S8 from 4 replicas of 500 ns MD simulations). The collective variables are selected as the vertical distance from the atom of interest to the center of mass of LCO. (a-e) show atoms from NADH, (f) from NICO, and (g-h) from RIBO. See Fig. 6 for the definition of atom types.

not well captured for RIBO as shown in Fig. S9 in **Supporting Information**, which leads to a higher level of uncertainty in the binding affinity. Nevertheless, it is clear that RIBO shows much more favorable adsorption compared to NADH groups, while NICO shows a negligible degree of adsorption. The lack of accessibility of NICO to the surface limits its chance of participating in redox reactions with LCO, which is a possible explanation of the experimental observation.[10]

4   Concluding Remarks

To better understand the properties of the LCO-solution interface, such as the binding of small molecule solutes, we develop a classical force field model for the LCO (001) surface within the framework of the INTERFACE/CHARMM force fields. Specifically, the model is based on the force field recently developed for bulk LCO materials[25] and considers the surface termination pattern at neutral pH in water as predicted by recent DFT calculations.[36] We calibrate the model by comparing results for interfacial properties to *ab initio* molecular dynamics simulations with DFT, and then apply the model to study the binding behaviors of small molecules to the LCO surface in water. It is observed that the water molecules in close contact with the LCO surface form a strongly adsorbed layer, which leads to a free energy barrier for the binding of small molecules. Due to the strong hydrogen bonding interactions with the LCO surface, the first water layer forms an interface that exhibits hydrophobic characters, as observed in simulations of a few other polar or metallic solid/water interfaces. As a result, hydrophobic solutes, especially those featuring extended non-polar areas, are observed to bind to the first water layer at the LCO surface. In other words, despite its highly polar nature, the LCO (001) surface is expected to bind not only polar/charged but also non-polar solutes, and this characteristic needs to be taken into consideration for the analysis of chemistry at the LCO/water interface.

As the first application, the model is then used to analyze the adsorption of NADH

and its molecular components (RIBO and NICO) to the LCO (001) surface in water. It is observed that while both NADH and RIBO bind strongly to the LCO surface, NICO exhibits negligible degree of binding affinity. These results provide plausible explanation for the recent experimental finding[10] that while both NADH and RIBO enhanced ion dissolution from LCO, NICO was not significantly oxidized upon exposure to LCO. The observed redox activity of NADH at the LCO/water interface was therefore due to the co-operativity between the ribose component, which drives binding to the LCO surface, and the nicotinamide moiety, which undergoes oxidation.

The current force field model shares limitations as the conventional empirical models such as CHARMM and INTERFACE. For example, electronic polarization is not described explicitly, which may limit the reliability of the model in some applications.[62–64] In addition, it is observed that sodium ions exhibit fairly strong binding ($\sim 4\ k_B T$) to the oxygen terminating sites (see Fig. S7), which needs to be better calibrated using, for example, electrophoretic ζ potential and might require specific NBFIX terms[65] for surface-ion interactions. Finally, it should be emphasized that the interface can not be completely characterized with a classical model. Even within the 50 ps DFT simulation reported in this work, we observe spontaneous proton transfer between the LCO surface and nearby water molecules (see Fig. S10 for snapshots). Therefore, the chemistry at the LCO/solution interface can be rich in scope, and to properly describe these processes quantitatively requires further development of more complex potential functions based on QM/MM[62] or machine learning[20] approaches.

Acknowledgement

Nanoscale Accepted Manuscript

Supporting Information Available

Additional data used for the development of the force field model and analyses for the binding of small molecules to the LCO (001)/water interface are included. Also shown are snapshots along the *ab initio* molecular dynamics simulations that illustrate the spontaneous proton transfer between the LCO surface and nearby water molecules. This material is available free of charge via the Internet at `http://pubs.acs.org/`.

References

(1) Ho, M.; Khiew, P.; Isa, D.; Tan, T.; Chiu, W.; Chia, C. A review of metal oxide composite electrode materials for electrochemical capacitors. *Nano* **2014**, *9*, 1430002.

(2) Mei, J.; Liao, T.; Sun, Z. Two-dimensional metal oxide nanosheets for rechargeable batteries. *J. Energy Chem.* **2018**, *27*, 117–127.

(3) Mei, J.; Liao, T.; Kou, L.; Sun, Z. Two-dimensional metal oxide nanomaterials for next-generation rechargeable batteries. *Adv. Mater.* **2017**, *29*, 1700176.

(4) Hamers, R. J. Nanomaterials and global sustainability. *Acc. Chem. Res.* **2017**, *50*, 633–637.

(5) Zeng, X.; Li, J.; Liu, L. Solving spent lithium-ion battery problems in China: Opportunities and challenges. *Renew. Sust. Energ. Rev.* **2015**, *52*, 1759–1767.

(6) Hang, M. N.; Gunsolus, I. L.; Wayland, H.; Melby, E. S.; Mensch, A. C.; Hurley, K. R.; Pedersen, J. A.; Haynes, C. L.; Hamers, R. J. Impact of nanoscale lithium nickel manganese cobalt oxide (NMC) on the bacterium Shewanella oneidensis MR-1. *Chem. Mater.* **2016**, *28*, 1092–1100.

(7) Hang, M. N.; Hudson-Smith, N. V.; Clement, P. L.; Zhang, Y.; Wang, C.; Haynes, C. L.; Hamers, R. J. Influence of nanoparticle morphology on ion release and biological impact of nickel manganese cobalt oxide (NMC) complex oxide nanomaterials. *ACS Appl. Nano Mater.* **2018**, *1*, 1721–1730.

(8) Laudadio, E. D.; Ilani-Kashkouli, P.; Green, C. M.; Kabengi, N. J.; Hamers, R. J. Interaction of phosphate with lithium cobalt oxide nanoparticles: A combined spectroscopic and calorimetric study. *Langmuir* **2019**, *35*, 16640–16649.

(9) Laudadio, E. D.; Bennett, J. W.; Green, C. M.; Mason, S. E.; Hamers, R. J. Impact of phosphate adsorption on complex cobalt oxide nanoparticle dispersibility in aqueous media. *Environ. Sci. Technol.* **2018**, *52*, 10186–10195.

(10) Henke, A. H.; Laudadio, E. D.; Orbeck, J. K. H.; Tamijani, A. A.; Hoang, K. N. L.; Mason, S. E.; Murphy, C. J.; Feng, Z. V.; Hamers, R. J. Reciprocal redox interactions of lithium cobalt oxide nanoparticles with nicotinamide adenine dinucleotide (NADH) and glutathione (GSH): toward a mechanistic understanding of nanoparticle-biological interactions. *Environ. Sci. Nano* **2021**, *8*, 1749–1760.

(11) Nolan, A. M.; Zhu, Y.; He, X.; Bai, Q.; Mo, Y. Computation-accelerated design of materials and interfaces for all-solid-state lithium-ion batteries. *Joule* **2018**, *2*, 2016–2046.

(12) Giri, A.; Hopkins, P. E. A review of experimental and computational advances in thermal boundary conductance and nanoscale thermal transport across solid interfaces. *Adv. Funct. Mater.* **2020**, *30*, 1903857.

Nanoscale Accepted Manuscript

(13) Chakraborty, A.; Kunnikuruvan, S.; Kumar, S.; Markovsky, B.; Aurbach, D.; Dixit, M.; Major, D. T. Layered Cathode Materials for Lithium-Ion Batteries: Review of Computational Studies on $LiNi_{1-x-y}Co_xMn_yO_2$ and $LiNi_{1-x-y}Co_xAl_yO_2$. *Chem. Mater.* **2020**, *32*, 915–952.

(14) Mori, T.; Hamers, R. J.; Pedersen, J. A.; Cui, Q. An explicit consideration of desolvation is critical to binding free energy calculations of charged molecules at ionic surfaces. *J. Chem. Theory Comput.* **2013**, *9*, 5059–5069.

(15) Serva, A.; Salanne, M.; Havenith, M.; Pezzotti, S. Size dependence of hydrophobic hydration at electrified gold/water interfaces. *Proc. Natl. Acad. Sci. U.S.A.* **2021**, *118*.

(16) Hafner, J. Ab-initio simulations of materials using VASP: Density-functional theory and beyond. *J. Comput. Chem.* **2008**, *29*, 2044–2078.

(17) Bennett, J. W.; Allen, C.; Pramanik, S.; Gallagher, M. J.; Hudson-Smith, N. V.; Jones, D.; Krause, M. O.; Mason, S. E. Research highlights: comparing the biological response of nanoparticle solid solutions. *Environ. Sci. Nano* **2017**, *4*, 1428–1432.

(18) Wang, R.; Klein, M. L.; Carnevale, V.; Borguet, E. Investigations of water/oxide interfaces by molecular dynamics simulations. *Wiley Interdiscip. Rev. Comput. Mol. Sci.* **2021**, e1537.

(19) Kirchner, B.; di Dio, P. J.; Hutter, J. Real-world predictions from ab initio molecular dynamics simulations. *Multiscale Molecular Methods in Applied Chemistry* **2011**, 109–153.

(20) Schran, C.; Thiemann, F. L.; Rowe, P.; Müller, E. A.; Marsalek, O.; Michaelides, A. Machine learning potentials for complex aqueous systems made simple. *Proc. Natl. Acad. Sci. U.S.A.* **2021**, *118*, e2110077118.

(21) Behler, J. Four Generations of High-Dimensional Neural Network Potentials. *Chem. Rev.* **2021**, *121*, 10037–10072.

(22) A. D. MacKerell Jr.,; Bashford, D.; Bellott, M.; R. L. Dunbrack Jr.,; Evenseck, J. D.; Field, M. J.; Fischer, S.; Gao, J.; Guo, H.; Ha, S.; Joseph-McCarthy, D.; Kuchnir, L.; Kuczera, K.; Lau, F. T. K.; Mattos, C.; Michnick, S.; Ngo, T.; Nguyen, D. T.; Prodhom, B.; W. E. Reiher III,; Roux, B.; Schlenkrich, M.; Smith, J. C.; Stote, R.; Straub, J.; Watanabe, M.; Wiórkiewicz-Kuczera, J.; Yin, D.; Karplus, M. All-atom empirical potential for molecular modeling and dynamics studies of proteins. *J. Phys. Chem. B* **1998**, *102*, 3586–3616.

(23) Mackerell Jr, A. D.; Feig, M.; Brooks III, C. L. Extending the treatment of backbone energetics in protein force fields: limitations of gas-phase quantum mechanics in reproducing protein conformational distributions in molecular dynamics simulations. *J. Comput. Chem.* **2004**, *25*, 1400–1415.

(24) Cornell, W. D.; Cieplak, P.; Bayly, C. I.; Gould, I. R.; Merz, K. M.; Ferguson, D. M.; Spellmeyer, D. C.; Fox, T.; Caldwell, J. W.; Kollman, P. A. A second generation force field for the simulation of proteins, nucleic acids, and organic molecules. *J. Am. Chem. Soc.* **1995**, *117*, 5179–5197.

(25) Dhakane, A.; Varshney, V.; Liu, J.; Heinz, H.; Jain, A. Molecular dynamics simulations of separator-cathode interfacial thermal transport in a Li-ion cell. *Surf. Interfaces* **2020**, *21*, 100674.

(26) Giannozzi, P.; Andreussi, O.; Brumme, T.; Bunau, O.; Nardelli, M. B.; Calandra, M.; Car, R.; Cavazzoni, C.; Ceresoli, D.; Cococcioni, M.; Colonna, N.; Carnimeo, I.; Corso, A. D.; de Gironcoli, S.; Delugas, P.; Jr, R. A. D.; Ferretti, A.; Floris, A.; Fratesi, G.; Fugallo, G.; Gebauer, R.; Gerstmann, U.; Giustino, F.; Gorni, T.; Jia, J.; Kawamura, M.; Ko, H.-Y.; Kokalj, A.; Küçükbenli, E.; Lazzeri, M.; Marsili, M.;

Nanoscale Accepted Manuscript

Marzari, N.; Mauri, F.; Nguyen, N. L.; Nguyen, H.-V.; de-la Roza, A. O.; Paulatto, L.; Poncé, S.; Rocca, D.; Sabatini, R.; Santra, B.; Schlipf, M.; Seitsonen, A. P.; Smogunov, A.; Timrov, I.; Thonhauser, T.; Umari, P.; Vast, N.; Wu, X.; Baroni, S. Advanced capabilities for materials modelling with QUANTUM ESPRESSO. *J. Phys. Condens. Matter* **2017**, *29*, 465901.

(27) Giannozzi, P.; Baroni, S.; Bonini, N.; Calandra, M.; Car, R.; Cavazzoni, C.; Ceresoli, D.; Chiarotti, G. L.; Cococcioni, M.; Dabo, I.; Dal Corso, A.; de Gironcoli, S.; Fabris, S.; Fratesi, G.; Gebauer, R.; Gerstmann, U.; Gougoussis, C.; Kokalj, A.; Lazzeri, M.; Martin-Samos, L.; Marzari, N.; Mauri, F.; Mazzarello, R.; Paolini, S.; Pasquarello, A.; Paulatto, L.; Sbraccia, C.; Scandolo, S.; Sclauzero, G.; Seitsonen, A. P.; Smogunov, A.; Umari, P.; Wentzcovitch, R. M. QUANTUM ESPRESSO: a modular and open-source software project for quantum simulations of materials. *J. Phys. Condens. Matter* **2009**, *21*, 395502 (19pp).

(28) Tang, W.; Sanville, E.; Henkelman, G. A grid-based Bader analysis algorithm without lattice bias. *J. Phys. Condens. Matter* **2009**, *21*, 084204.

(29) Sanville, E.; Kenny, S. D.; Smith, R.; Henkelman, G. Improved grid-based algorithm for Bader charge allocation. *J. Comput. Chem.* **2007**, *28*, 899–908.

(30) Henkelman, G.; Arnaldsson, A.; Jónsson, H. A fast and robust algorithm for Bader decomposition of charge density. *Comput. Mater. Sci.* **2006**, *36*, 354–360.

(31) Perdew, J. P.; Burke, K.; Ernzerhof, M. Generalized gradient approximation made simple. *Phys. Rev. Lett.* **1996**, *77*, 3865.

(32) Hubbard, J. Electron correlations in narrow energy bands. *Proc. Math. Phys. Eng. Sci. P ROY SOC A-MATH PHY* **1963**, *276*, 238–257.

(33) Bennett, J. W.; Hudson, B. G.; Metz, I. K.; Liang, D.; Spurgeon, S.; Cui, Q.; Ma-

son, S. E. A systematic determination of hubbard U using the GBRV ultrasoft pseudopotential set. *Comput. Mater. Sci.* **2019**, *170*, 109137.

(34) Vanderbilt, D. Soft self-consistent pseudopotentials in a generalized eigenvalue formalism. *Phys. Rev. B* **1990**, *41*, 7892.

(35) Garrity, K. F.; Bennett, J. W.; Rabe, K. M.; Vanderbilt, D. Pseudopotentials for high-throughput DFT calculations. *Comput. Mater. Sci.* **2014**, *81*, 446–452.

(36) Huang, X.; Bennett, J. W.; Hang, M. N.; Laudadio, E. D.; Hamers, R. J.; Mason, S. E. Ab initio atomistic thermodynamics study of the (001) surface of $LiCoO_2$ in a water environment and implications for reactivity under ambient conditions. *J. Phys. Chem. C* **2017**, *121*, 5069–5080.

(37) Abbaspour-Tamijani, A.; Bennett, J. W.; Jones, D. T.; Cartagena-Gonzalez, N.; Jones, Z. R.; Laudadio, E. D.; Hamers, R. J.; Santana, J. A.; Mason, S. E. DFT and thermodynamics calculations of surface cation release in $LiCoO_2$. *Appl. Surf. Sci.* **2020**, *515*, 145865.

(38) Gao, F.; Han, L. Implementing the Nelder-Mead simplex algorithm with adaptive parameters. *Comput. Optim. Appl.* **2012**, *51*, 259–277.

(39) Virtanen, P.; Gommers, R.; Oliphant, T. E.; Haberland, M.; Reddy, T.; Cournapeau, D.; Burovski, E.; Peterson, P.; Weckesser, W.; Bright, J.; van der Walt, S. J.; Brett, M.; Wilson, J.; Millman, K. J.; Mayorov, N.; Nelson, A. R. J.; Jones, E.; Kern, R.; Larson, E.; Carey, C. J.; Polat, İ.; Feng, Y.; Moore, E. W.; VanderPlas, J.; Laxalde, D.; Perktold, J.; Cimrman, R.; Henriksen, I.; Quintero, E. A.; Harris, C. R.; Archibald, A. M.; Ribeiro, A. H.; Pedregosa, F.; van Mulbregt, P.; SciPy 1.0 Contributors, SciPy 1.0: Fundamental Algorithms for Scientific Computing in Python. *Nat. Methods* **2020**, *17*, 261–272.

Nanoscale Accepted Manuscript

Nanoscale Accepted Manuscript

(40) Brooks, B. R.; III, C. L. B.; Mackerell, A. D.; Nilsson, L.; Petrella, R. J.; Roux, B.; Won, Y.; Archontis, G.; Bartels, C.; Boresch, S.; Caflisch, A.; Caves, L.; Cui, Q.; Dinner, A. R.; Feig, M.; Fischer, S.; Gao, J.; Hodoscek, M.; Im, W.; Kuczera, K.; Lazaridis, T.; Ma, J.; Ovchinnikov, V.; Paci, E.; Pastor, R. W.; Post, C. B.; Pu, J. Z.; Schaefer, M.; Tidor, B.; Venable, R. M.; Woodcock, H. L.; Wu, X.; Yang, W.; York, D. M.; Karplus, M. CHARMM: The Biomolecular Simulation Program. *J. Comput. Chem.* **2009**, *30*, 1545–1614.

(41) Darden, T.; York, D.; Pedersen, L. Particle mesh Ewald: An Nlog (N) method for Ewald sums in large systems. *J. Chem. Phys.* **1993**, *98*, 10089–10092.

(42) Lippert, G.; Hutter, J.; Parrinello, M. A hybrid Gaussian and plane wave density functional scheme. *Mol. Phys.* **1997**, *92*, 477–487.

(43) Kḧne, T. D.; Iannuzzi, M.; M. Del Ben,; Rybkin, V. V.; Seewald, P.; Stein, F.; Laino, T.; Khaliullin, R. Z.; Schütt, O.; Schiffmann, F.; Golze, D.; Wilhelm, J.; Chulkov, S.; Bani-Hashemian, M. H.; Weber, V.; Borstnik, U.; Taillefumier, M.; Jakobovits, A. S.; Lazzaro, A.; Pabst, H.; Müller, T.; Schade, R.; Guidon, M.; Andermatt, S.; Holmberg, N.; Schenter, G. K.; Hehn, A.; Bussy, A.; Belleflamme, F.; Tabacchi, G.; Glöβ, A.; Lass, M.; Bethune, I.; Mundy, C. J.; Plessl, C.; Watkins, M.; J. VanderVondele,; Krack, M.; Hutter, J. CP2K: An electronic structure and molecular dynamics software package-Quickstep: Efficient and accurate electronic structure calculations. *J. Chem. Phys.* **2020**, *152*, 194103.

(44) Ehrlich, S.; Moellmann, J.; Reckien, W.; Bredow, T.; Grimme, S. System-dependent dispersion coefficients for the DFT-D3 treatment of adsorption processes on ionic surfaces. *Chem. Phys. Chem.* **2011**, *12*, 3414–3420.

(45) Phillips, J. C.; Hardy, D. J.; Maia, J. D. C.; Stone, J. E.; Ribeiro, J. V.; Bernardi, R. C.; Buch, R.; Fiorin, G.; Henin, J.; Jiang, W.; McGreevy, R.; Melo, M. C. R.; Radak, B. K.;

Skeel, R. D.; Singharoy, A.; Wang, Y.; Roux, B.; Aksimentiev, A.; Luthey-Schulten, Z.; Kale, L. V.; Schulten, K.; Chipot, C.; Tajkhorshid, E. Scalable molecular dynamics on CPU and GPU architectures with NAMD. *J. Chem. Phys.* **2020**, *153*, 044130.

(46) Jorgensen, W. L.; Chandrasekhar, J.; Madura, J. D.; Impey, R. W.; Klein, M. L. Comparison of simple potential functions for simulating liquid water. *J. Chem. Phys.* **1983**, *79*, 926–935.

(47) Neria, E.; Fischer, S.; Karplus, M. Simulation of activation free energies in molecular systems. *J. Chem. Phys.* **1996**, *105*, 1902–1921.

(48) Noskov, S. Y.; Roux, B. Control of Ion Selectivity in LeuT: Two Na$^+$ Binding Sites with Two Different Mechanisms. *J. Mol. Biol.* **2008**, *377*, 804–818.

(49) Luo, Y.; Roux, B. Simulation of Osmotic Pressure in Concentrated Aqueous Salt Solutions. *J. Phys. Chem. Lett.* **2010**, *1*, 183–189.

(50) Landau, L.; Lifshitz, E. Statistical Physics, v. 5. *Course of Theoretical Physics* **1980**, *23*.

(51) Laio, A.; Gervasio, F. L. Metadynamics: a method to simulate rare events and reconstruct the free energy in biophysics, chemistry and material science. *Rep. Prog. Phys.* **2008**, *71*, 126601.

(52) Barducci, A.; Bussi, G.; Parrinello, M. Well-tempered metadynamics: a smoothly converging and tunable free-energy method. *Phys. Rev. Lett.* **2008**, *100*, 020603.

(53) Price, D. J.; Brooks III, C. L. A modified TIP3P water potential for simulation with Ewald summation. *J. Chem. Phys.* **2004**, *121*, 10096–10103.

(54) Toukan, K.; Rahman, A. Molecular-dynamics study of atomic motions in water. *Phys. Rev. B* **1985**, *31*, 2643.

(55) Berendsen, H.; Grigera, J.; Straatsma, T. The missing term in effective pair potentials. *J. Phys. Chem.* **1987**, *91*, 6269–6271.

(56) Vanommeslaeghe, K.; Hatcher, E.; Acharya, C.; Kundu, S.; Zhong, S.; Shim, J.; Darian, E.; Guvench, O.; Lopes, P.; Vorobyov, I.; Mackerell, A. D. CHARMM general force field: A force field for drug-like molecules compatible with the CHARMM all-atom additive biological force fields. *J. Comput. Chem.* **2010**, *31*, 671–690.

(57) Andrade, M. F. C.; Ko, H.-Y.; Zhang, L.; Car, R.; Selloni, A. Free energy of proton transfer at the water–TiO$_2$ interface from ab initio deep potential molecular dynamics. *Chem. Sci.* **2020**, *11*, 2335–2341.

(58) Chew, A. K.; Dallin, B. C.; Van Lehn, R. C. The Interplay of Ligand Properties and Core Size Dictates the Hydrophobicity of Monolayer-Protected Gold Nanoparticles. *ACS Nano* **2021**, *15*, 4534–4545.

(59) Willard, A. P.; Chandler, D. The molecular structure of the interface between water and a hydrophobic substrate is liquid-vapor like. *J. Chem. Phys.* **2014**, *141*, 18C519.

(60) Nalbach, M.; Raiteri, P.; Klassen, S.; Schafer, S.; Gale, J. D.; Bechstein, R.; Kuhnle, A. Where Is the Most Hydrophobic Region? Benzopurpurine Self-Assembly at the Calcite–Water Interface. *J. Phys. Chem. C* **2017**, *121*, 24144–24151.

(61) Patel, A. J.; Varilly, P.; Jamadagni, S. N.; Hagan, M. F.; Chandler, D.; Garde, S. Sitting at the edge: How biomolecules use hydrophobicity to tune their interactions and function. *J. Phys. Chem. B* **2012**, *116*, 2498–2503.

(62) Cui, Q.; Hernandez, R.; Mason, S. E.; Frauenheim, T.; Pedersen, J. A.; Geiger, F. Sustainable nanotechnology: opportunities and challenges for theoretical/computational studies. *J. Phys. Chem. B* **2016**, *120*, 7297–7306.

(63) Dasetty, S.; Meza-Morales, P. J.; Getman, R. B.; Sarupria, S. Simulations of interfacial processes: recent advances in force field development. *Curr. Opin. Chem. Eng.* **2019**, *23*, 138–145.

(64) Kognole, A. A.; Aytenfisu, A. H.; MacKerell, A. D. Balanced polarizable Drude force field parameters for molecular anions: phosphates, sulfates, sulfamates, and oxides. *J. Mol. Model.* **2020**, *26*, 1–11.

(65) Venable, R. M.; Luo, Y.; Gawrisch, K.; Roux, B.; Pastor, R. W. Simulations of anionic lipid membranes: development of interaction-specific ion parameters and validation using NMR data. *J. Phys. Chem. B* **2013**, *117*, 10183–10192.

(66) Towns, J.; Cockerill, T.; Dahan, M.; Foster, I.; Gaither, K.; Grimshaw, A.; Hazelwood, V.; Lathrop, S.; Lifka, D.; Peterson, G. D.; Roskies, R.; Scott, J. R.; Wilkins-Diehr, N. XSEDE: Accelerating Scientific Discovery. *Comput Sci. & Engn.* **2014**, *16*, 62–74.

Nanoscale Accepted Manuscript